Beam Characterization of Linac 4's IS03

Daniel Noll, Jean-Baptiste Lallement, Alessandra Lombardi

Summary

After the second LHC long shutdown, Linac4 will become the new injector for proton beams to CERN's chain of accelerators. It has been commissioned at a maximum beam current of 25 mA, below the initial specification of 40 mA. At present, the beam current delivered by the linac is limited by the pre-injector. Previous investigations have found that this is due to the emittance of the H$^-$ beam extracted from the ion source exceeding the acceptance of the RFQ.

Detailed measurements of the beam parameters provided by the ion source at a dedicated test stand confirmed these earlier findings. By extending and adjusting the simulation model implemented using IBsimu, an agreement to the measured emittance values was obtained. An analysis of the simulation results shows that the larger-than-expected emittance is a result of aberration at the extraction electrodes. These are due to a plasma meniscus significantly more convex than predicted by the earlier simulation.

Three modifications to the extraction gap were proposed to achieve a shift of the plasma meniscus back towards a more concave position. Two of the changes—a shorter extraction gap and a larger bore diameter—result in significant decreases of the emittance as confirmed by experiments.

1 Introduction

Linac4 is a normal conducting linac, 80 m in length, delivering 160 MeV H$^-$ ions for charge-exchange injection into the CERN Proton Synchrotron Booster (PSB). It will become the sole provider of protons for the CERN accelerator complex in 2020, at the end of the second long shutdown (LS2). The 5 m long pre-injector consists of a 2 MHz RF ion source [1], a low-energy beam transport line (LEBT) and a Radio Frequency Quadrupole (RFQ) resonating at 352.2 MHz. It produces 850 μs long beam pulses at 3 MeV at a 0.8 Hz repetition rate. The low-energy front-end is followed by a Medium Energy Beam Transport line (MEBT), housing a fast chopper, and 22 radio-frequency (RF) structures of 3 different types (Drift Tube Linac (DTL), Cell Coupled-DTLs and Pi-mode structures) bringing the beam to its final energy.

Since its commissioning was completed in 2016 [2], the linac has been running with a maximum peak current of 25 mA, representing only 60 % of the nominal current, 45 mA [3]. Nevertheless, the beam intensity provided today at 160 MeV is sufficient to produce all the

different PSB proton beams as made with the retired Linac2. With a reduced current of 20 mA, both the reference high-brilliance LHC beam and the high intensity beams, dedicated to fixed target experiments, can be provided by respectively injecting 45 and 150 turns per PSB ring (including a 20 % safety margin) [4].

Although the present Linac4 ion source was shown capable of producing beam currents larger than 60 mA, since the beam emittance at high currents exceeds the acceptance of the RFQ by several factors, only a maximum beam current of approximately 30 mA has been obtained at 3 MeV so far. In order to study and improve the brilliance of the extracted beam, a dedicated test stand is operated in parallel with the ultimate goal of attaining 45 mA peak current out of the RFQ in 2023. Studies and measurements reported in this document refer to the test stand activities in the period from April 2017 to December 2018.

After an introduction of the source in section 2 and of the test stand, along with the methods used to analyze various measurements, in section 3, section 4 presents a set of measurements characterizing the beam extracted from the source in the initial configuration. Simulations of the extraction help in analyzing the measurement results: section 5 introduces the simulation model as well as the adjustments made. In section 6, the simulation results are analyzed for sources of emittance growth. Guided by simulations, three configurations with slightly changed geometries have been installed and measured. These will be motivated and discussed in section 7.

2   The present Linac4 ion source

Linac4's IS03 ion source is composed of a ceramic plasma chamber with an external five-turn antenna. Hydrogen gas is injected by a pulsed valve; a 2 MHz RF-amplifier provides up to 100 kW power for ignition of the plasma. The source can operate both in volume production mode, producing several 10's of milliamperes at electron to ion ratios of 20 and above, as well as in surface mode, after a one-time injection of cesium vapour, with ion currents up to 60 mA and electron to ion ratios close to 1.

The extraction system of IS03 consists of a five electrode system as shown in Figure 1. Its design is described in [5]. The beam is extracted through a bore with a diameter of 6.5 mm by an electric field generated by a dual-purpose puller-dump electrode. This electrode also houses a dump for the electrons co-extracted with the H^- beam. The beam is then accelerated to its final energy of 45 keV by an electrode connected to ground. To bridge the distance of approximately 20 cm between the ground electrode and the first focusing magnet in the LEBT, an accelerating einzel lens focuses the beam.

The puller-dump was typically operated at voltages between 5 kV to 12 kV, in relation to the plasma electrode. Outside of this range, signs of the electron beam missing the dump were observed, e.g. very high currents to ground triggering the current over-protection of the power supply which cuts short the beam pulse. Sparking was rarely observed, even at the higher limit of 12 kV. The lens was operated at a voltage of 30 kV. Higher values caused regular breakdowns.

The source is surrounded by a set of cusp magnets that provide plasma confinement. A pair of magnets placed shortly before the plasma bore produce a vertical magnetic dipole field that serves to deflect higher energy electrons back into the plasma. This filter field reduces
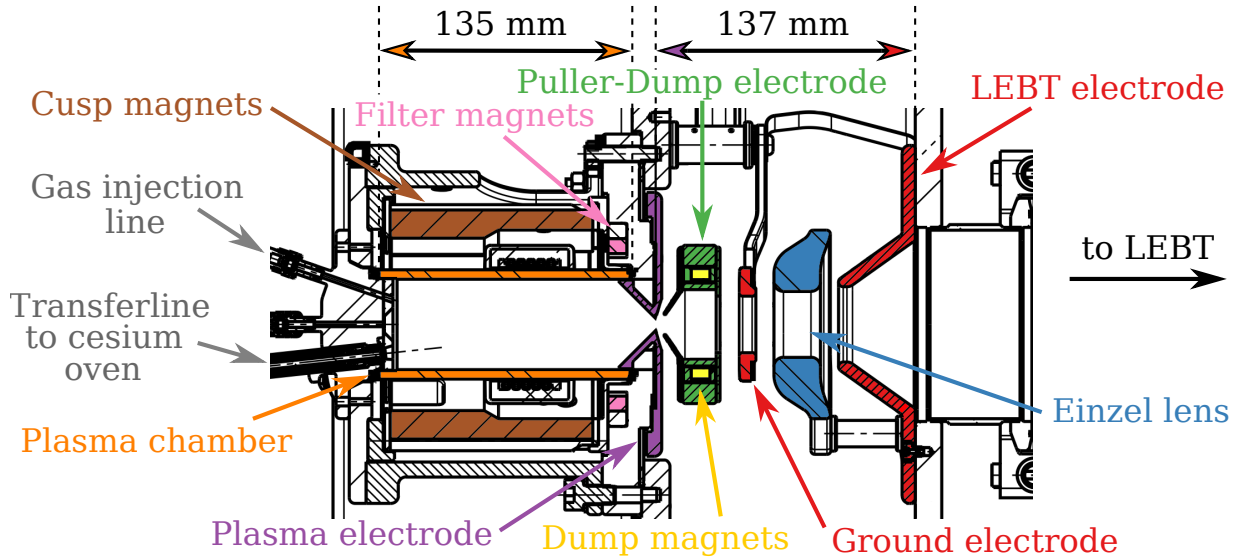
Figure 1: A schematic of Linac4's ion source IS03 [1].

the electron temperature in front of the extraction gap [6] which decreases the destruction rate of H$^-$ due to electron impact, thus both increasing the H$^-$ yield and suppressing the co-extraction of electrons.

The co-extracted electrons are deflected into a cup inside the puller-dump electrode by another magnetic dipole field, the dump field, generated by two permanent magnets housed inside the electrode itself. In order to minimize the influence of the dump field on the filter field and to postpone the onset of deflection until the beam reaches the dump, the side of the puller-dump electrode facing the plasma electrode contains an iron plate for magnetic shielding.

Filter and dump fields significantly deflect the H$^-$ beam. The central trajectory typically exits the extraction with an angle between 25 and 35 mrad, depending on the applied voltages. Both on the test stand as well as on Linac4, the front-end of the source containing the complete extraction system is tilted to compensate for this deflection. For technical reasons, the angle is limited to approximately 24 mrad, and is thus too low in most cases. The residual deflection is corrected downstream the source using two pairs of LEBT steerers, located after the first and in front of the second solenoid.

In operation, the ion source produces beam pulses with a length of up to 850 µs at a repetition rate of 0.8 Hz. The beam pulse length is controlled by the length of the RF pulse, with the bias voltage being switched on about 400 µs before the RF for stabilization.

An example of the beam current over the pulse, measured by a beam current transformer (BCT), is given in Figure 3. Some beam is already extracted during the ignition and stabilization phase of the plasma. Since neither current nor the beam properties are stable during this time, on Linac4, the first 150 µs are chopped by a pre-chopper in the LEBT. Another 100 µs of beam is then chopped after the RFQ, at 3 MeV, to remove the transient due to the onset of space charge compensation.

The ion source was measured on a dedicated test stand in various configurations. A list of configurations and when these were measured is given in Table 1.
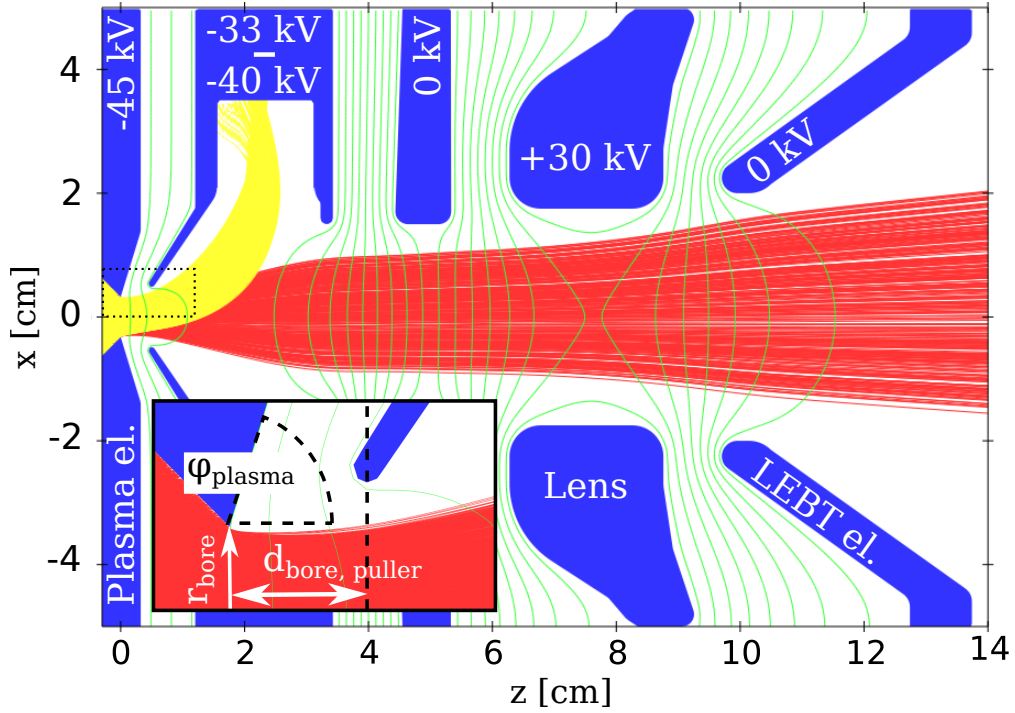
3

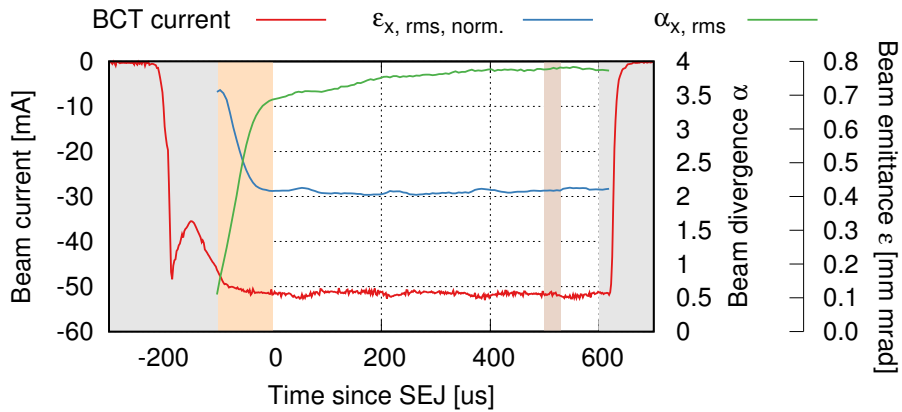Figure 2: The electrode layout of the IS03 extraction system.

Figure 3: Example for a beam pulse with beam current and beam parameters extracted from an emittance measurement taken on the Linac4 test stand (in configuration #6, Table 1). The gray areas indicate the times where the beam would be chopped by the pre-chopper before the RFQ in Linac4, the orange area indicates where the beam would be chopped after the RFQ. All beam parameters given in this document were extracted in during the times marked in brown.
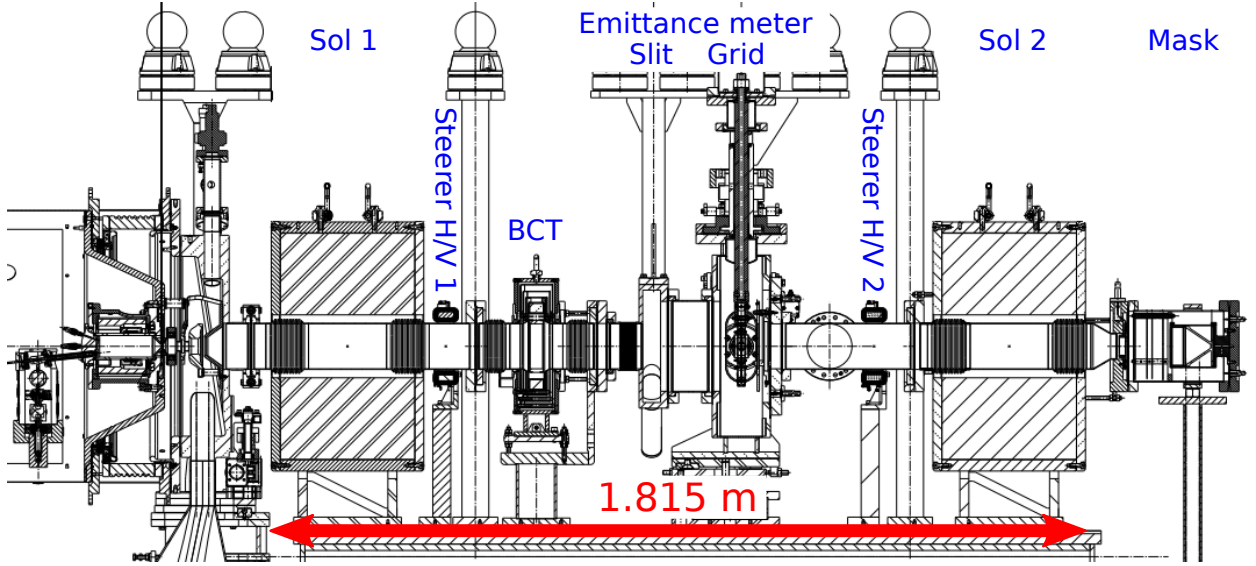
4

Figure 4: Layout of the Linac4 test stand in the setup since July 2018.

3 The Linac 4 test stand: setup and measurement analysis

The Linac4 test stand shown in Figure 4 allows the characterization of ion sources before the installation on the accelerator and for machine development purposes.

The beam line starts with the ion source under test mounted on a front end, followed by the first LEBT solenoid. A pair of steerer magnets allows for re-centering of the beam. A BCT provides a measurement of the beam current. Up to this point, the setup at the test stand is identical to the setup on Linac4.

Downstream of the BCT, the beam's transverse emittances can be measured using a slit-and-grid emittance meter. A plate with two slits, one in vertical and one in horizontal direction, is mounted on a motor and can be inserted into the beam line in a 45° angle, measuring in a range of ± 35 mm around the axis. 20 cm downstream of the slit two grids with 40 wires each spaced by 0.75 mm can be inserted depending on the measurement plane. Therefore, a range of 149 mrad in angles can be measured. The emittance meter is gated in 6 µs steps, allowing a time resolved measurement over the beam pulse.

#	Cesiation	$d_{\text{bore,puller}}$	$2r_{\text{bore}}$	φ_{plasma}	Measurements
1	Yes	4.5 mm	6.5 mm	73°	August 2017
2	No	4.5 mm	6.5 mm	73°	June 2018
3	No	3.5 mm	6.5 mm	73°	June 2018
4	No	3.5 mm	6.5 mm	60°	July 2018
5	No	3.5 mm	7.5 mm	73°	July 2018
6	Yes	3.5 mm	7.5 mm	73°	December 2018

Table 1: Configurations of the source measured at the Linac4 test stand. Various dimensions in the extraction gap of the source, which are defined in Figure 2, were changed.
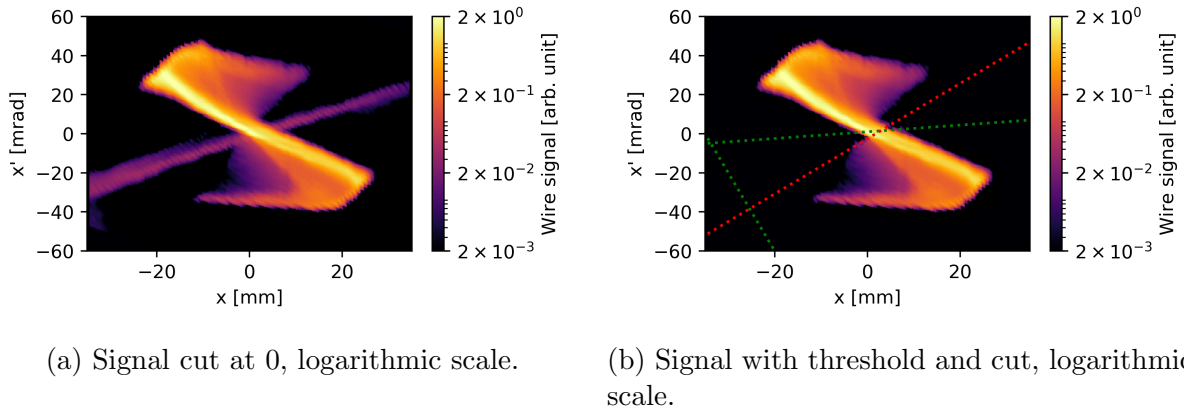
(a) Signal cut at 0, logarithmic scale.

(b) Signal with threshold and cut, logarithmic scale.

Figure 5: A measurement in configuration #5: 42 mA, e/H=43). Signals not belonging to the H⁻ beam are removed in areas between by two lines in which a low threshold is applied.

All measurements presented here were taken with a transverse resolution of 0.75 mm, requiring approx. 45 min per measurement.

Various spurious signals are present in the emittance measurements which have to be removed before beam parameters can be calculated. Figure 5 gives an example of a raw measurement in comparison to the cleaned-up signal used for emittance calculation. The signal along the diagonal is caused by fast neutral particles—their orientation in phase space is not influenced by any change in the solenoid current. Additionally, a signal of low level appears in the lower left corner for measurements in the horizontal plane and in the upper right corner for the vertical plane. This signal is due to beam passing through the slit intended for measurements in the other plane.

These signals always appear in the same positions, independent on the source state. They can be automatically removed unless the real beam signal overlaps these regions. Avoiding an overlap can usually be achieved by choosing proper settings of the solenoid and the steerers. For the analysis, a threshold is applied in the area defined by two lines as indicated in Figure 5b. This threshold is carefully chosen for each set of measurements not to disturb the core of the beam. Threshold values typically used are in the few percent range of the maximal signal. Since the threshold is only applied locally and not globally, features at smaller signals remain intact.

The grid of the emittance meter works in a secondary emission mode, where each impinging H⁻ particle produces a number of secondary electrons on the grid's wires. The secondary electrons are then accelerated away from the grid by a positively biased metallic ring into beam pipe downstream of the emittance meter. The signal measured is thus positive. Nevertheless a small amount of electrons is able to cross the distance between two wires and is registered as a small negative current. This cross-talk between wires depends on the bias high voltage.

Figure 6 provides a comparison of two emittance measurements of the same beam with the high voltage switched off and on, at the reference value of 1000 V. Without bias voltage, the (positive) beam signal is significantly cut away by the appearance of a negative background in the order of several percent of the maximum beam signal. In the example, most of the wings of the beam as well as the signal of the neutral particles disappear in the vicinity of

the H$^-$ beam. This background is suppressed to below a percent of the maximum beam signal at 1 kV.
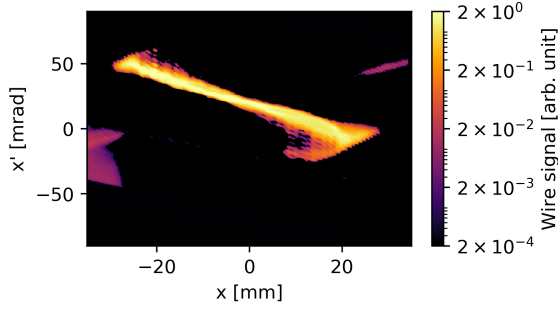
The negative background has a large influence on the rms emittance values calculated from the measurement, depending on the position of the beam and on the presence of areas with low signal values. When the emittance is high there are a lot of wires that carry low currents which are heavily affected by the cross-talk. Thus a large contribution in phase-space area can disappear in the background when the bias is switched off. When the emittance is small, only a few wires carry most of the beam signal and the impact is smaller. Figure 6e gives the emittance as a function of beam current for a source configuration not further discussed in this document, measured with the bias voltage both on and off. The emittances displayed in (a)-(d) are taken from the highest current in (e). In this case, the value without bias voltage is 40 % lower than with the voltage switched on. For the cases with lower emittance, the difference is in the order of 10 %.

All measurements where done with 1 kV bias, except for those for configuration #6, where the cables were erroneously left unconnected.

Between June 2017 and October 2018 various improvements to both the measurement procedure as well as the analysis were made:

- With beams with small angular spread, the situation can occur that most of the beam passes between two wires of the emittance meter grid at some slit positions. This causes holes in the signal of the beam at some positions. To mitigate this problem, at each slit position, there are two acquisitions on the grid, one with the grid offset by half the wire spacing. This effectively doubles the angular resolution of the measurement. All data presented in this report were taken using this improvement.

- Initially, measurements could only be launched individually through a graphical interface implemented in Labview. An implementation in Python using the same FESA class as the Labview application made it possible to automate a series of measurements.

- Previously, when one of the high voltage power supplies went into a faulty state and needed to be reset, the measurement continued and thus contained incomplete data. The new implementation waits for a reset, resumes the measurement and, if necessary, reacquires missed data.

- For each beam pulse measured by the emittance meter, measurements of other relevant source data (BCT current trace, traces from the RF amplifier and the high voltage power supplies, ...) were stored in additional files, documenting the source state during the emittance measurement. These files can later be analyzed to provide more exact values of various parameters, for example electron to ion ratio, as well as their evolution during the measurement.

As previously described, Linac4 requires beam pulses of up to 600 µs with constant beam current and distribution. In measurement and operation, careful—and in many cases manual—tuning of the RF power and frequency as well as of the timing of the gas injection are required to achieve a flat beam pulse. Since this tuning was not always feasible in the (automatic) acquisition of various parameters, in the following, measurements are always taken at the end of the beam pulse. The corresponding time window is marked in brown in
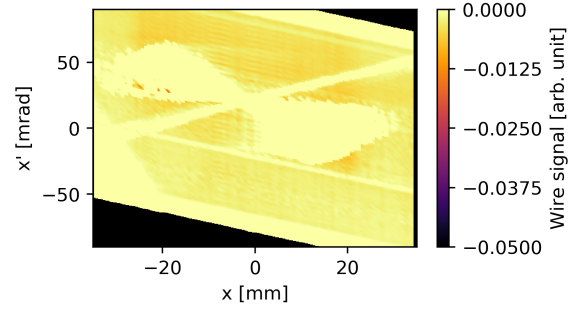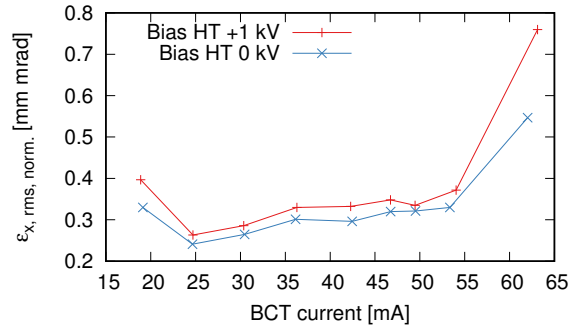
7
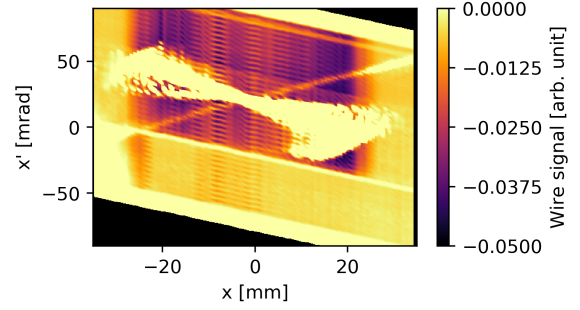
(a) 0 V, beam signal.

(b) 0 V, negative background.
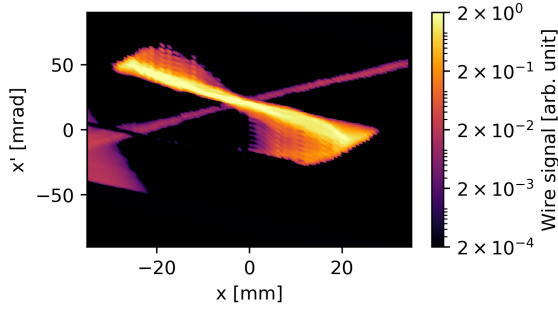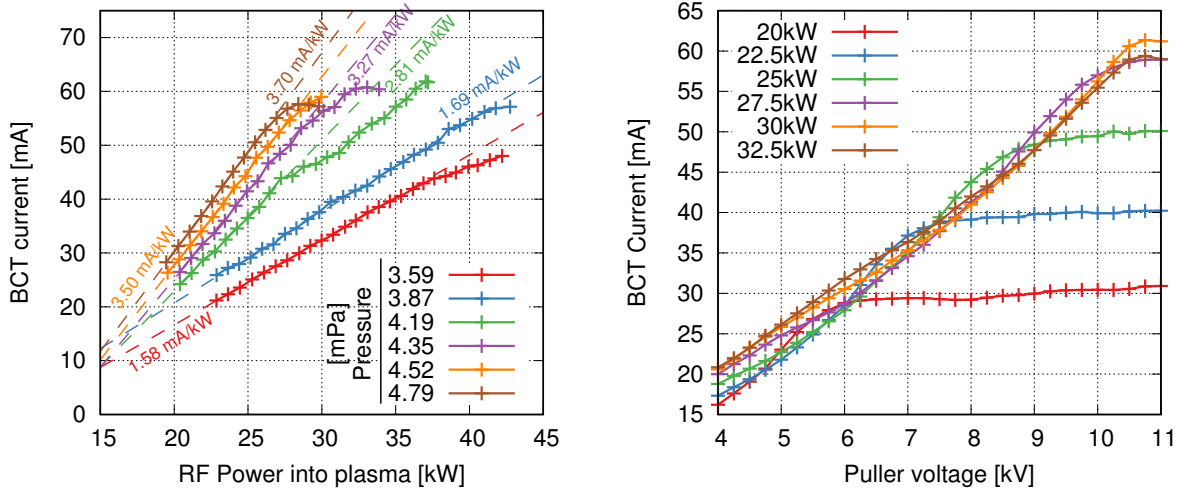

(c) 1000 V, beam signal.

(d) 1000 V, negative background.

(e) Influence of the bias voltage at various currents & emittances.

Figure 6: Influence of the emittance meter bias voltage. The figures in (a)-(d) are for the highest current in (e). For this measurement, normalized RMS emittances are equal to 0.55 mm mrad when the voltage is switched off and to 0.76 mm mrad at 1000 V.

(a) Example for the influence of the gas injection and the rf power, at constant 10 kV puller voltage. Note that the linear fits do not intersect 0 mA at 0 kW.

(b) Example for the influence of the puller voltage for the highest pressure acquisition value in (a).

Figure 7: Three source parameters have a significant influence of the current extracted from the source: rf power, the amount of gas injected and the puller voltage. Note that due to the difficulties involved, the pressure values given are measured not in the plasma chamber (but in the pump tank below the extraction and at a later time) and thus only give a trend for the pressure during the presence of the plasma.

Figure 3. The assumption is that the source can always be tuned to achieve the measured values over the full pulse, which might not be the case in certain extreme cases.

4   Source characterization

Figure 7 gives an example of the dependence of the beam current measured in the BCT on three critical parameters: the power transmitted into the plasma, the amount of gas injected and the puller voltage. Measurements were taken briefly after the cesiation of the source in configuration #1 (Table 1). The solenoid was set to a current of 100 A which is sufficient to transport all of the beam to the BCT.

In a given range, the measured beam current is proportional to the RF power transmitted into the plasma. This can be seen in Figure 7a, which was measured at a constant puller voltage. Towards 60 mA, independent on the pressure, the current saturates or even decreases with further increase of the rf power. The H$^-$ yield per power can be controlled by the level of gas injection. In this measurement, higher pressures and thus higher yields could not be reached due to a strong increase of sparks in the extraction gap.

This additionally affects the electron to ion ratio, which varied between approximately 1.2 and 2.5 in the curves in Figure 7a, increasing with the pressure. On the uncesiated sources, the influence of the pressure on the electron to ion ratio is more pronounced, easily increasing by 10 to 20 over the usable range. Thus, operation at the lowest pressure at which

9
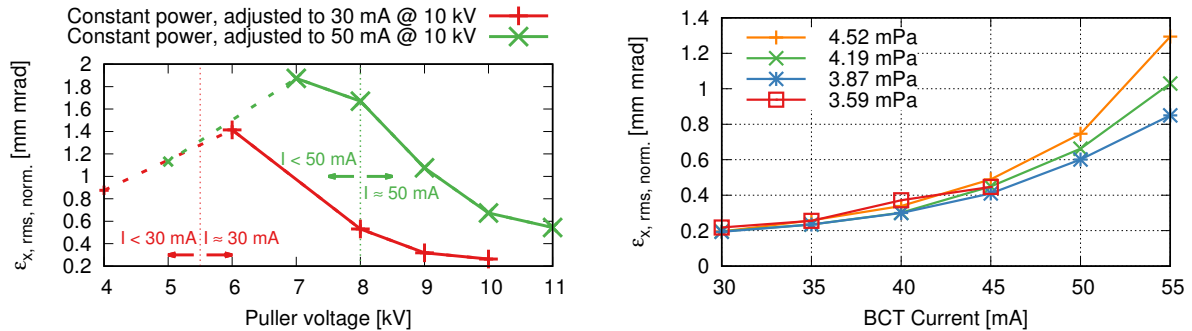
(a) Scan of the puller voltage at constant rf power resulting at 30 mA and 50 mA at 10 kV. e/H ratio was approx. 4.

(b) Emittance as a function of beam current at constant levels of gas injection and constant puller voltage (10 kV). e/H was between 2 and 3.

Figure 8: Emittance measurements of configuration #1.

the wanted current can be achieved is usually beneficial.

Figure 7b gives an example for the beam current as a function of the puller voltage. Up to a certain voltage, the measured current increases and reaches a plateau at a current level, depending on the amount of gas injected (not shown) and the rf power. The same current limit of 60 mA can be observed in this measurement. Both the limit at high power and voltage, as well as the behaviour below the plateau are due to aperture restrictions as will be shown later in comparison with simulation.

Along these curves, i.e. as a function of beam current and puller voltage, emittance measurements were taken.

The beam emittance grows significantly with beam current, as shown in Figure 8. For the measurements given in this document, these scans are always given at a constant puller voltage of 10 kV. There is also an influence of the level of gas injection on the emittance. Whether this is just a result of an increase in the electron to ion ratio or if there are additional effects will be investigated in future measurements.

Due to different setups and differences in the analysis of the measurement, these are difficult to compare to emittances given for other H$^-$ ion sources. Nevertheless, the results at large currents are much higher than either the design goal (0.25 mm mrad normalized rms emittance at 50 mA and e/H=3 [5]) or values found in the literature for other sources. For the extraction system of the J-PARC H$^-$ source, values of approximately 0.26 mm mrad are given in [7, Figure 3] for a current of 66 mA and 0.2 mm mrad for a current of 40 mA in [8, Figure 10] (albeit at a higher beam energy of 50 keV and with 5 % signal cut-off). SNS reports a value of 0.22 mm mrad at 50 mA and at a beam energy of 65 keV in [9, Figure 5]. Neither the different threshold values nor the differences in extraction energy seem large enough to explain a factor 2-3 higher emittance.

The influence of the puller voltage is given in Figure 8 for two beam currents. For this source configuration, choosing the highest possible puller voltage results in the lowest possible emittance. The emittance increases rapidly towards lower puller voltage, especially at the higher beam current. This increase is a result of the appearance of "wings" in the emittance figures, which will be discussed and explained later. The highest emittance values were

10

observed around the voltages below which the current starts to drop significantly. Extracting at even lower voltage, the emittances decrease again. This is due to measurement error: the beam size is too large and exceeds the measurement range of the emittance meter.

The presented emittance scans serve as a benchmark for simulations. Scans of the puller voltage are useful since for these the plasma parameters such as the densities and temperatures inside the source volume are not changed. This is no longer the case when the rf power is changed.

5 Simulation of the beam extraction

The extraction system was modeled in IBsimu [10] which was already used extensively in the design of the system [5, 11]. The magnetic fields of the dump and the filter magnets were calculated using Opera from the previously existing model.

The tilt of the front end was not implemented in the simulation since it was found to have only a small influence on the beam parameters such as the emittance and divergence. The solenoid field was adjusted to correspond to a current of $100\,\mathrm{A}$ ($66.5\,\mathrm{mT\,m}$) as typically used in the measurements.

After the final gap of the einzel lens, the external electric fields are low enough for the beam to trap ions generated by ionizing collisions with the residual gas (space charge compensation). In the past, backtracking studies have indicated that almost a full compensation of the beams space charge is reached at the end of the pulse [12, 13]. For this reason, the simulation assumes $100\,\%$ space charge compensation starting from $z = 14\,\mathrm{cm}$.

5.1 Convergence studies

For negative ion beams, the differential equation solved by IBsimu [14] is

$$
\begin{aligned}
-\epsilon_0 \nabla^2 \varphi(\mathbf{r}) &= \rho_{\mathrm{neg}}(\mathbf{r}) + \rho_{\mathrm{th}}(\mathbf{r}) && + \rho_{\mathrm{f}}(\mathbf{r}) \\
&= \rho_{\mathrm{neg}}(\mathbf{r}) + \rho_{\mathrm{th0}} \exp\left(-\frac{e\varphi(\mathbf{r})}{k_b T_p}\right) + \rho_{\mathrm{f0}}\left(1 - \mathrm{erf}\left(\frac{\varphi(\mathbf{r})}{\varphi_p}\right)\right).
\end{aligned}
\tag{1}
$$

Three contributions add up to the total charge density. The negative charge density ρ_{neg} contains the charge density from the ion beam as well as of the co-extracted electrons. These are calculated by tracking particles through the system. Particle tracking and solutions of Equation 1 are then alternated until the solutions converge.

In the plasma region up to the presence of the extraction field, the negative charges are assumed to be compensated by two types of particles which are included in the space charge solver and not tracked: a thermally distributed species ρ_{th} at temperature T_p which models the plasma and a contribution ρ_{f} from fast particles at the plasma potential φ_p. Quasi-neutrality in the plasma dictates that all contributions to the charge density add up to zero, $\rho_{\mathrm{neg0}} + \rho_{\mathrm{f0}} + \rho_{\mathrm{th0}} = 0$, where ρ_{neg0} is $\rho_{\mathrm{neg}}(\mathbf{r})$ somewhere in the plasma with $\nabla^2 \varphi(\mathbf{r}) = 0$. Therefore, ρ_{neg} can be distributed between the fast and the thermal ion species, $\rho_{\mathrm{f0}} = R_{\mathrm{f}} \rho_{\mathrm{neg0}}$ and $\rho_{\mathrm{th0}} = (1 - R_{\mathrm{f}}) \rho_{\mathrm{neg0}}$.

An example for the behaviour of these quantities is given in Figure 9, for a beam current of $50\,\mathrm{mA}$ with no additional electrons. The meniscus in this case is slightly concave and
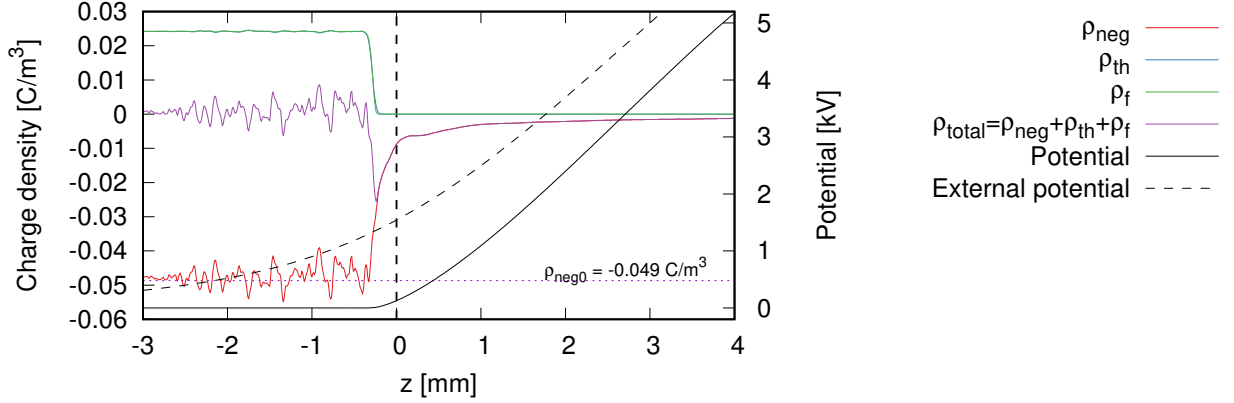
Figure 9: An example for the potential and densities on the axis in the extraction region, for a 70 mA beam in IBsimu. Since $R_f = 0.5$, ρ_{th} and ρ_f reach the same value in the plasma and only differ imperceptibly at the meniscus.

Parameter		Value
Transverse temperature	T_t	0.5 eV
Initial particle energy	E_0	5 eV
Plasma temperature	T_p	1 eV
Plasma potential	φ_p	7.5 V
Fast/Thermal ion mixing	R_f	0.5

Figure 10: Plasma model parameters.

located before the bore at $z = 0$ cm. The external potential i.e. the potential of the system without plasma or charged particles extends far into the plasma region. This potential is fully compensated to zero before the meniscus, located approximately 200 µm in front of the bore. Downstream, the positive compensating components ρ_{th} and ρ_f drop sharply as the potential rises from 0 V. At this point there is significant excess of negative charges due to the low velocity of the H⁻ ion.

Equation 1 without the contribution of the fast particles ($R_f = 0$) has a characteristic length, the Debye length

$$\lambda_d = \sqrt{\frac{\epsilon_0 k_b T_p}{e \rho_{neg0}}}. \tag{2}$$

When space is rescaled as $\tilde{\mathbf{r}} = \mathbf{r}/\lambda_d$ and the potential as $\tilde{\varphi} = e\varphi/(k_b T_p)$, Equation 1 becomes

$$-\tilde{\nabla}^2 \tilde{\varphi}(\tilde{\mathbf{r}}) = \frac{\rho_{neg}(\mathbf{r})}{\rho_{neg0}} - \exp(-\tilde{\varphi}),$$

which only contains dimensionless variables. Solutions of this equation with a rapid change in charge density, such as at the plasma meniscus, will show changes on the scale of the Debye length. For an accurate solution, the mesh resolution should thus be chosen in the order of λ_d.

Introducing the charge density of an H⁻ beam with a current of I_{H^-} extracted along with
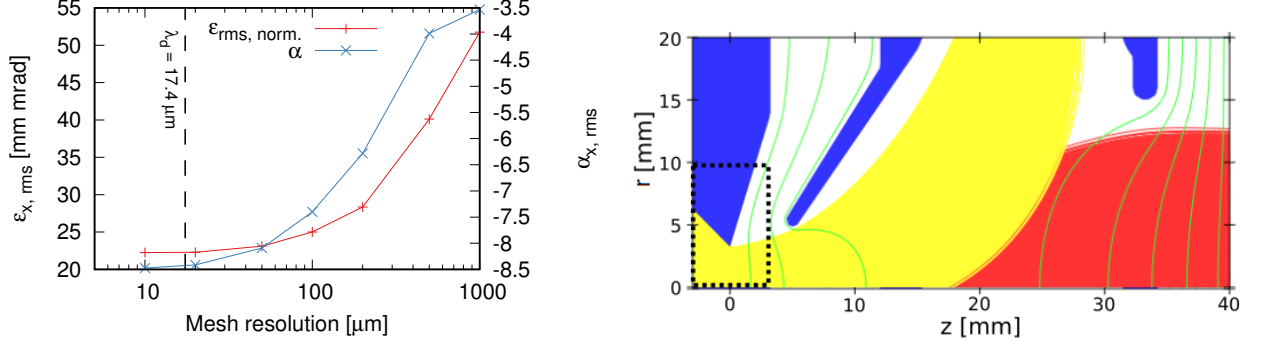
(a) RMS beam parameter α and the beam emittance after $2\,\text{cm}$ of the extraction system simulated at various grid resolutions in cylindrical geometry. $30\,\text{mA}$ H^- are extracted at $10\,\text{kV}$ with no additional electrons. Convergence is observed for resolutions below the Debye length λ_d (3).

(b) Simulation domains in the presented simulations. The area where the field is calculated in cylindrical coordinates is marked by the dashed rectangle. The rest of the extraction is calculated in 3D.

Figure 11: The IBsimu simulation only converges when the Debye length of the plasma is resolved. A two-dimensional cylindrical grid in the plasma region allows reaching the required resolutions.

$I_{e^-} = k I_{H^-}$ electrons, both at an initial energy of E_0, the Debye length is

$$\lambda_d = R_{\text{bore}} \sqrt{\frac{\epsilon_0 k_b T_p \pi}{e I_{\text{SC}}} \sqrt{\frac{2E_0}{m_{H^-}}}} \quad \text{with} \quad I_{\text{SC}} = I_{H^-} \left(1 + \sqrt{\frac{m_{e^-}}{m_{H^-}}} k \right). \tag{3}$$

I_{SC} is the charge density equivalent H^- current of both the H^- and the electrons. The quantity will later also be useful for analysis of the measurements. Figure 11a contains the rms divergences and emittances of an $I = 30\,\text{mA}$ beam with no co-extracted electrons after $2\,\text{cm}$ for various grid resolutions. The simulations were performed in cylindrical geometry. For these parameters—all others as given in Figure 10—the Debye length is $\lambda_d = 17.4\,\mu\text{m}$. At mesh sizes larger than this value, significant changes in the rms quantities are observed.

Considering only the meniscus region, in three dimensions, simulations in this resolution become impractical due to a very large number of mesh cells. We adopted a scheme where the extraction up to $4\,\text{mm}$ after the plasma bore is calculated on a cylindrical mesh. The area calculated at high resolution is indicated in Figure 11b. Per iteration, the following steps are performed:

1. Calculate the electric field in the full extraction in 3D.

2. Calculate the electric field in the plasma region up to $4\,\text{mm}$ after the bore in cylindrical geometry. The field from the 3D solver is used as a boundary condition at this position.

3. Track a beam in the cylindrical geometry, not considering the magnetic fields.

4. Track a beam in 3D using the field from the cylindrical solver, where calculated, and the field from the 3D solver otherwise.

13
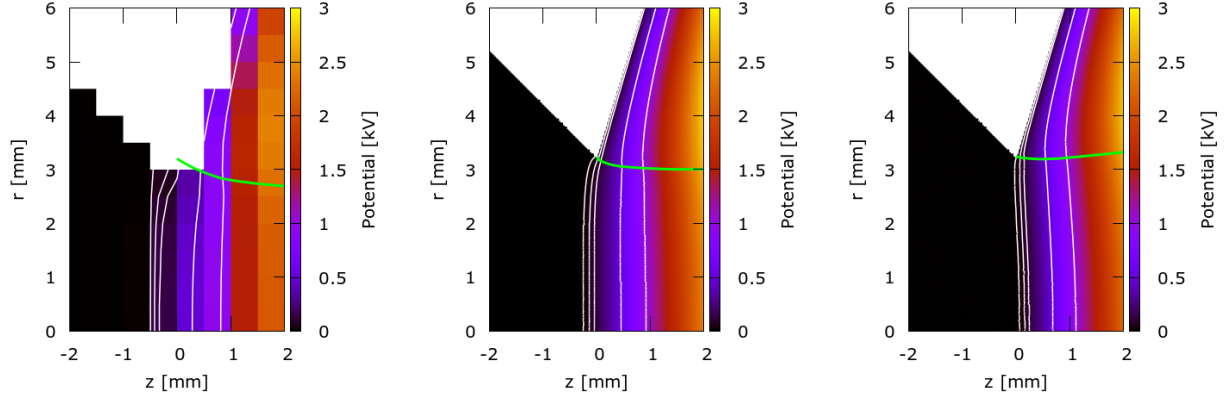
(a) Without rz mesh, $\rho_{\text{neg,corr.}}/\rho_{\text{neg}} = 0\%$.

(b) With rz mesh, $\rho_{\text{neg,corr.}}/\rho_{\text{neg}} = 0\%$.

(c) With rz mesh, $\rho_{\text{neg,corr.}}/\rho_{\text{neg}} = 30\%$.

Figure 12: Comparison of the plasma meniscus location and shape. White lines are equipotential lines at 0, 10, 50, 100, 500 V, 1 kV and 5 kV, increasing from left to right. The green line indicates the envelope of the beam. Simulation resolution in (a) was 500 μm and 10 μm in (b) and (c).

Thus, we assume the plasma meniscus to be radially symmetric i.e. we neglect the influence of the deflection of the beam on the electric field in the first 4 mm. Additionally, as particles tracked in three dimension start to be deflected by the magnetic field, they will see a slightly incorrect electric field. The average deflection after 4 mm is in the range of one to a few 100 μm.

Figure 13 contains a comparison of beam emittance and divergence between two simulations with and without the cylindrical mesh along with measurement results. A resolution of 10 μm was used for the rz mesh, while both simulations used a three dimensional mesh with 500 μm resolution for the rest of the source. Increasing the resolution shifts the plasma meniscus into a less concave position—an example of the charge density distribution with and without cylindrical mesh is given in Figure 12a and Figure 12b respectively—leading to a larger emittance growth downstream and a shift of the simulated curve towards the measurement.

5.2 Adjustment to measurements

While investigating the influence of various parameters in the simulation, we observed that simulation results for much higher electron to ion ratios than measured matched that of the measurements [15]. For example, during the measurement in Figure 13 the electron to ion ratio was around 4. This data agrees well to results from simulations at an electron to ion ratio of 20. There are two ways in which a higher electron to ion ratio affects the beam in the simulation:

1. by causing emittance growth due to asymmetric dumping of the electrons.
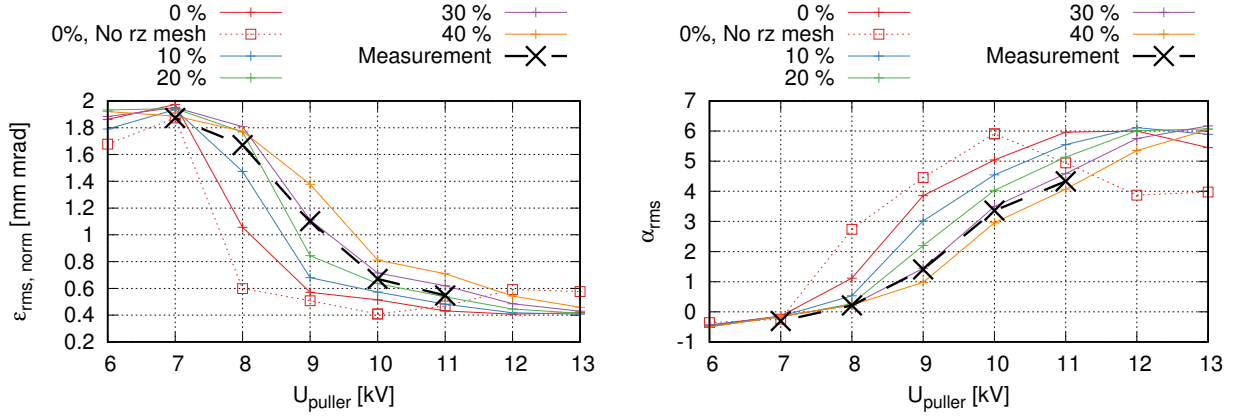
(a) Normalized rms beam emittance ϵ_{rms}.

(b) RMS beam divergence α_{rms}.

Figure 13: Dependence of emittance and divergence of a $50\,\mathrm{mA}$ beam (dashed black curve) in comparison to various simulations. During the measurement the electron to ion ratio varied between 3.4 and 4.4 with an average of 3.9. For all simulations, a value of 4 was used. The dotted curves are taken from simulations without the refined mesh around the plasma bore. The colored curves are simulation with different density scaling $\rho_{\mathrm{neg,corrected}}/\rho_{\mathrm{neg}}$ in the plasma region.

2. by increasing the negative charge density in the plasma,

$$\rho_{\mathrm{neg}}(\mathrm{e/H} = 20) / \rho_{\mathrm{neg}}(\mathrm{e/H} = 4) = 1.35,$$

which causes a shift in the plasma meniscus and therefore changes the initial beam distribution.

The electron and the ion beams overlap in the first $2.5\,\mathrm{cm}$ of the extraction. At an electron current of $1\,\mathrm{A}$ and an H^- current of $50\,\mathrm{mA}$, according to the simulation, the emittance growth in this area is below $5\,\%$. Thus, aberration due to the asymmetric bending of the electron beam is not the cause for the larger emittances and the observed agreement between simulation and measurement.

The increased charge density at higher electron to ion ratios will also significantly change the position of the plasma meniscus. However, an error in the measurement of the electron to ion ratio in the order of 15 is deemed highly unlikely. Therefore, it was concluded that instead of the measurement of the electron current being incorrect, the estimate of the plasma density in the simulation was not accurate. Thus, to achieve the same results at the measured electron to ion ratio in the simulation, a mechanism was implemented that increases the charge density within the plasma region by a given factor $\rho_{\mathrm{neg,corrected}}/\rho_{\mathrm{neg}}$.

The influence of this factor on the emittance and beam divergence at the emittance meter can be seen in Figure 13. At $30\,\%$, the simulation accurately predicts both the beam's emittance as well as its divergence. At this value, the plasma meniscus as shown in Figure 12c is slightly convex instead of concave, leading to a moderately defocused beam in the extraction gap.

After these tests at Linac4, a revisit of emittance data from 2016 by the author of IBsimu has yielded an adjustment factor of $50\,\%$ [16]. The higher value could result from

(a) Normalized rms beam emittance ϵ_{rms}.

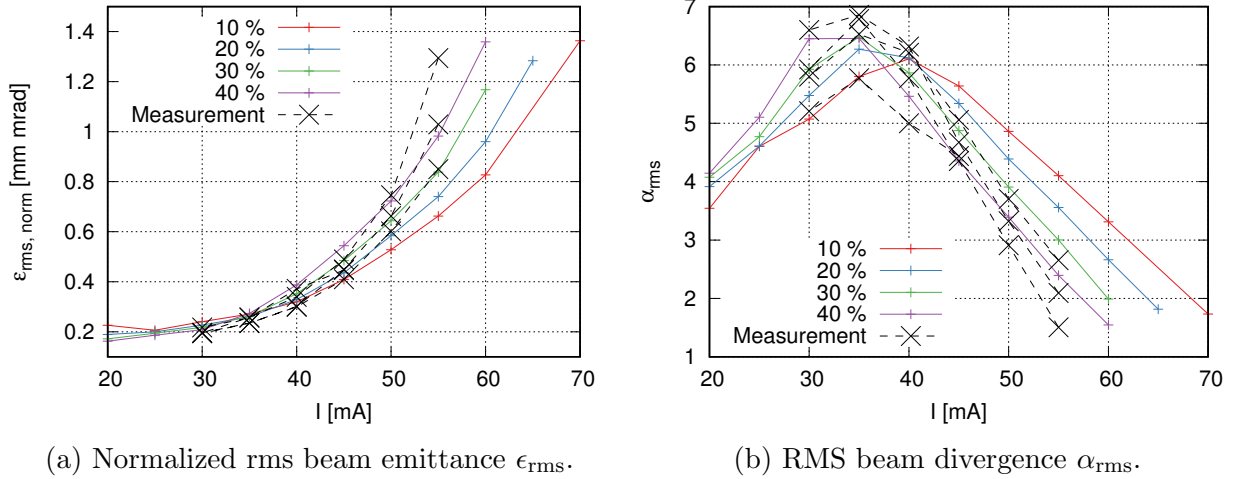(b) RMS beam divergence α_{rms}.

Figure 14: Influence of the beam current on emittance and divergence in a comparison between simulation and measurement. During the measurement, the electron to ion ratio was on average between 2 and 3. Puller voltage constant at $10\,\mathrm{kV}$. Simulations shown were performed with an e/H ratio of 2.

compensating the influence of the insufficient mesh resolution by an increase in plasma density.

In Figure 14, the influence of the beam current on the beam parameters is compared between measurements and simulations with different density enhancement factors. For the lower beam currents that were measured, emittances calculated from simulations with different $\rho_{\mathrm{neg,corrected}}/\rho_{\mathrm{neg}}$ all fit the measurements equally well. However, the simulations deviate at higher beam currents. If the density in the plasma region is not increased for these cases, the predicted emittances are too low. Again, an increase of $30\,\%$ provides a reasonable match. Additionally, at this value, the simulations reproduce the maximum in α_{rms} around $35\,\mathrm{mA}$ which is shifted towards higher currents when the density is left uncorrected.

Simulations were also performed for measurements done for an uncesiated source. In this case, the electron to ion ratio depends strongly on the level of gas injection and the rf power, and is not known a priori. As as input for the simulation, the electron current of those measurements with the lowest electron to ion ratio at a given beam current were fitted using an exponential function $aI_{\mathrm{H}^-}^n + b$. The beam parameters at the emittance meter, given in Figure 15, fit the measured values remarkably well at the previously found adjustment factor.

6 Analysis of the simulation: beam transmission and emittance growth

While the need for the density increase factor is not yet understood—likely a result of an incomplete model in IBsimu—, the simulation can be used to understand the origins of emittance growth in the present extraction system.

Figure 17 shows the rms beam emittances calculated at various points in the extraction
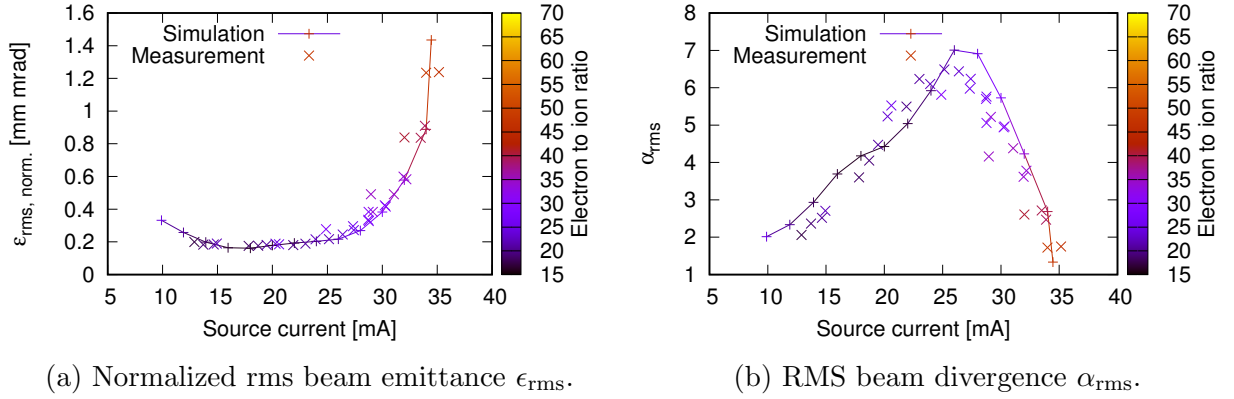
(a) Normalized rms beam emittance ϵ_{rms}.

(b) RMS beam divergence α_{rms}.

Figure 15: Comparison of a simulation with $\rho_{\mathrm{neg,corrected}}/\rho_{\mathrm{neg}} = 30\,\%$ to measurements in volume mode with 6.5 mm bore diameter and a puller-to-plasma electrode distance of 3.5 mm. The electron to ion ratios used as input to the simulation were taken from an arbitrary fit to the measured value of the electron current ($I_{\mathrm{e^-}}(I_{\mathrm{H^-}}) = 1\,\mathrm{A}\,(I_{\mathrm{H^-}}/33.1\,\mathrm{mA})^{4.6342} + 250\,\mathrm{mA}$).
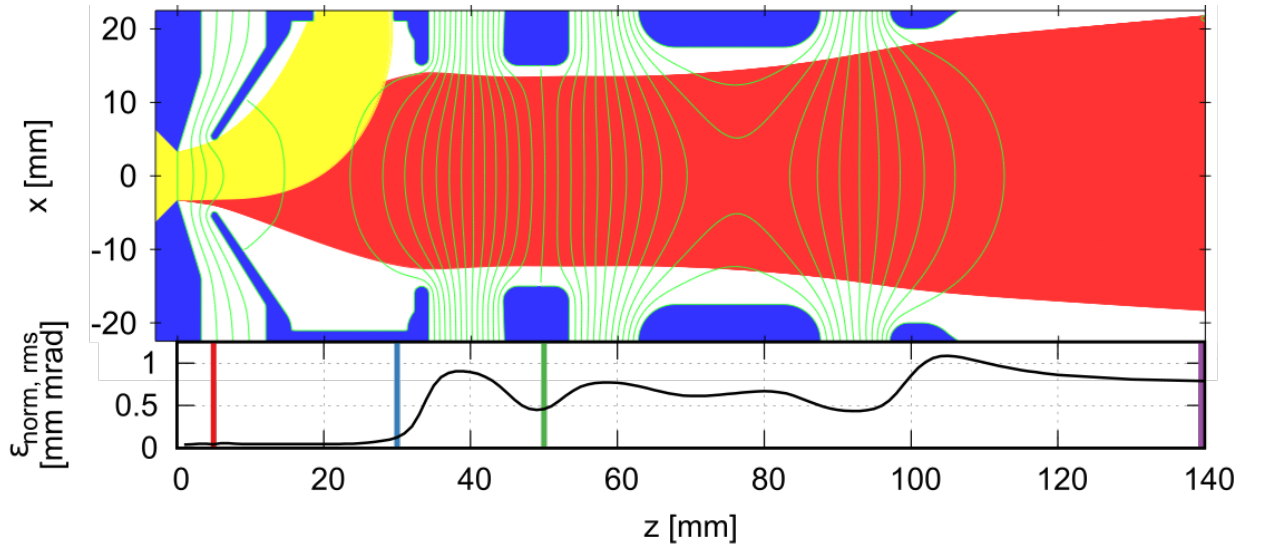
Figure 16: For high current beams (here, $55\,\mathrm{mA}$, $U_{\mathrm{puller}} = 10\,\mathrm{kV}$ and e/H of 2), the beam fills most of the available aperture, causing aberration in regions with large transverse electric fields. The most significant points are at the aperture of the end-plate of the puller-dump, which acts as a focusing lens, and at the LEBT electrode.

17
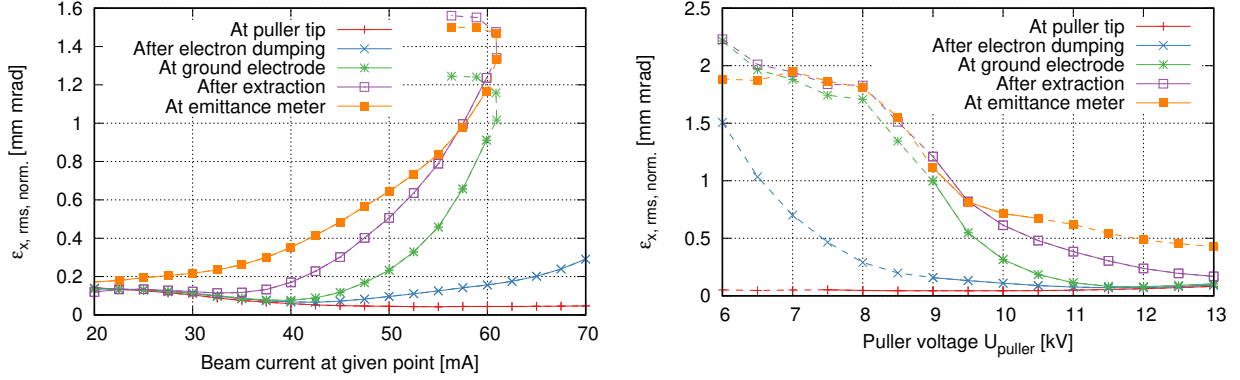
(a) Emittance ϵ_{rms} at various locations in the extraction as a function of beam current at these positions, at a 10 kV puller voltage.

(b) Emittance at various locations in the extraction as a function of puller voltage, 50 mA beam current and e/H$^-$ratio of 4.

Figure 17: Emittances at different positions in the extraction system where the beam energy of all particles are approximately equal: before the end plate of the puller-dump electrode, at the center of the ground electrode, after the extraction and at the emittance meter. Dashed lines indicated a total transmission below 99 %.

system in the two situations previously matched to simulations (Figure 13 and Figure 14). The positions are marked and color-coded in Figure 16, which gives an example of the evolution of the rms emittance evolution for 55 mA beam current.

The initial value of the emittance calculated at the tip of the puller electrode is extremely low. For $U_{\mathrm{puller}} = 10\,\mathrm{kV}$, the minimum $\epsilon_{\mathrm{rms,norm.}}$=0.045 mm mrad along the curves in Figure 17 is located at $I_{\mathrm{H}^-} = 50\,\mathrm{mA}$. A significant increase of the emittance at this position occurs only towards low beam currents: due to the low space charge density, the meniscus becomes very concave, resulting in non-linear focusing of particles at the edge of the bore. The same effect causes the slight increase in emittance visible in Figure 17b towards high puller voltages.

This situation—too high extraction field in relation to the beam current—leaves a clear signature in the phase-space distribution of the beam. An example from measurement and simulation is given in Figure 18. At the edge of the bore, particles are focused differently by the electric field than those in the core due to the highly concave meniscus. This separate beam component is already visible at the edge of the beam in the charge density shortly after extraction depicted in (c). These particles then result in a halo that is transported very differently from the rest of the beam through the system. In the emittance measurement shown in (a), they are visible as "fins" with almost the same orientation in phase space as the rest of the beam. This distribution is well reproduced by the simulation. Note that the plots of the phase-space densities in (a) and (b) have been scaled to cover the same dynamic range and that the wings have the same strength in relation to the signal maximum in measurement as in simulation. Displaying the particle distribution color coded by the radius of the origin of the particle confirms that these wings are indeed caused by the aberration at the bore. In less extreme cases, the effect produces small wings close to the axis that are less focused than the rest of the beam.
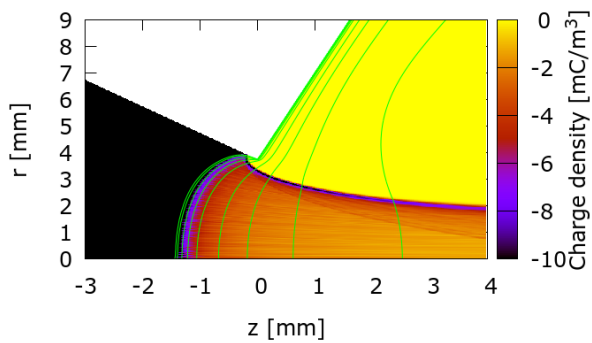
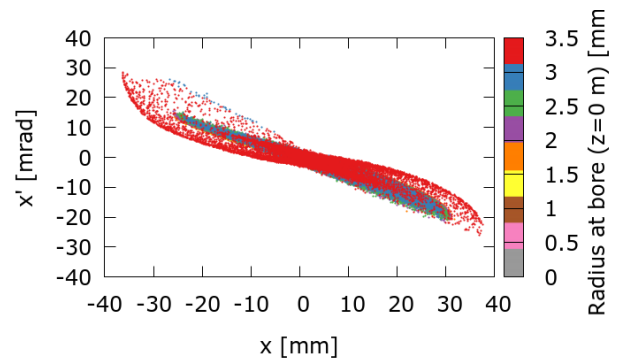Within the puller-dump electrode, the emittance only grows by a few percent compared to
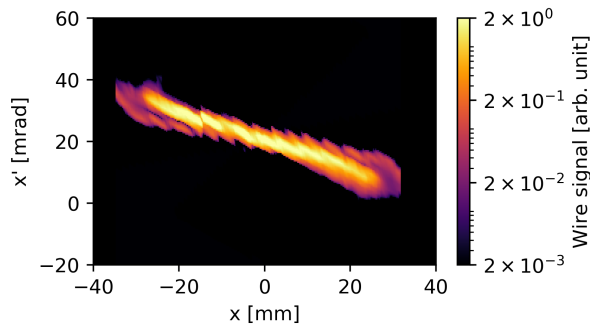
(a) Emittance measurement.
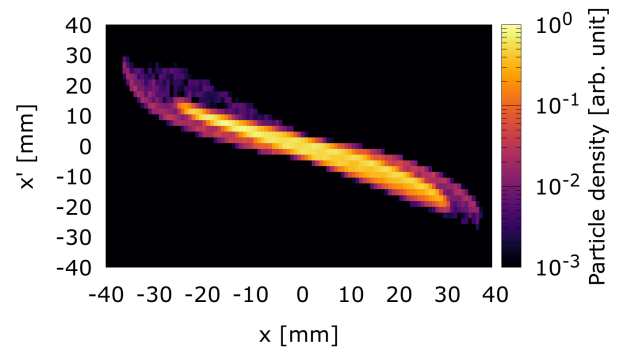
(b) Distribution at emittance meter from simulation.

(c) Charge density around the bore. Equipotential lines in green (10 V, 20 V, 50 V, 100 V, ...).

(d) Distribution from (b), color coded with particle radius at the bore

Figure 18: Extraction with a too large extraction field in measurement and simulation: The emittance figure shows "wings" that can be shown to be emitted from the edge of the plasma electrode bore.
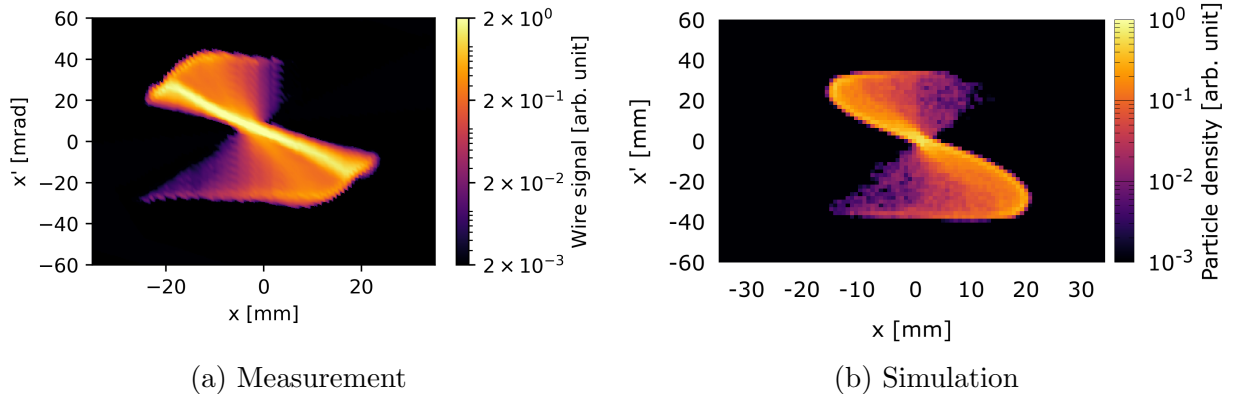
19

(a) Measurement   (b) Simulation

Figure 19: Appearance of "wings" in the emittance figures for $50\,\mathrm{mA}$ and $U_{\mathrm{puller}} = 9\,\mathrm{kV}$ in configuration #1.

the value at the emittance meter. The influence of the asymmetric dumping of the electron beam on the H^- beam is therefore negligible. Even when electron currents reach several amperes, a similar conclusion can be drawn from the simulation of the uncesiated source.

Both in simulations with high effective beam current as well as in simulations with low extraction voltages, a great fraction of the emittance growth occurs at the plate at the end of the puller-dump electrode facing the ground electrode. Due to the large aperture of this end-plate ($3\,\mathrm{cm}$), the accelerating field penetrates far into the dump region. Non-linear radial field components cause the emittance to grow if the beam fills this aperture significantly. This is the case, both at low extraction voltages as well as for the higher currents, where the meniscus is concave.

A beam close to the end-plate of the puller electrode causes the appearance of large area but low density "wings" in the emittance figures. An example is given in Figure 19b. Similar structures can be found in measurements, such as in Figure 19a. However, in measurements where the current was changed, this kind of "wing" tends to appear already at lower beam currents than in simulation. This discrepancy could either be due to an incorrect initial beam distribution or the occurrence of further losses in the measurement, both cutting the distribution into shape as well as causing a misreading of the initially extracted current.

For currents between 40 and $50\,\mathrm{mA}$, the einzel lens causes the largest increase in emittance, also due to the larger-than-expected beam radius. As the beam enters the solenoid with a large divergence comparable to the transverse momentum imparted by its fringe field, there is further emittance growth. This amounts to an increase by another $0.2\,\mathrm{mm}\,\mathrm{mrad}$, especially where no other strong mechanism of emittance growth is present.

Additionally, the end of the puller dump is also the first element limiting the beam current. Above an H^- current of $62\,\mathrm{mA}$ extracted from the plasma, the beam is collimated. This is identical to the value that has been previously been found in measurements of the beam current as a function of the puller voltage and rf power. Collimation is also the reason for the behaviour of these curves at low puller voltages: the simulated example for $50\,\mathrm{mA}$ shows losses at the end of the puller dump below $9\,\mathrm{kV}$. The simulation also predicts the occurrence of beam loss at puller voltages above $10.5\,\mathrm{kV}$. These have not been observed in the measurements up to a voltage of $11\,\mathrm{kV}$, but are clearly present in the measurements with
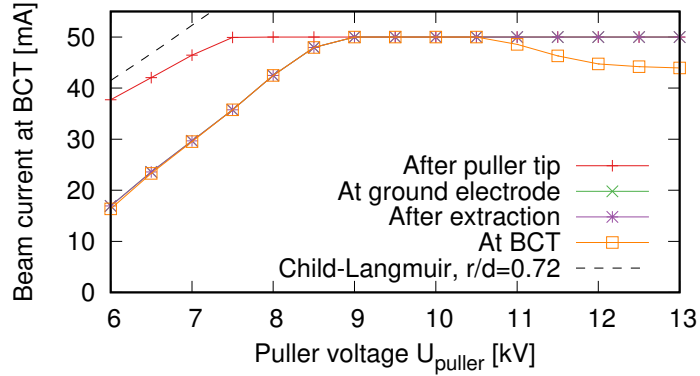
20

Figure 20: Simulation of the beam current as a function of puller voltage. The initially extracted current used as an input in IBsimu is 50 mA. The previously measured behaviour is caused by collimation at the puller electrode at low voltages.

larger bores as discussed below.

7 Mitigation

The previously mentioned adjustments to the IBsimu simulation, required for an improved fit to emittance measurements, cause the meniscus to be more convex than initially assumed. Therefore, any modification that causes the meniscus to be more concave is likely to improve the emittance since it causes the extracted beam to be closer in parameters to the beam initially assumed in the design of the extraction. Three modifications were investigated and the resulting electrodes tested on the Linac4 test stand.

In the following sections, all the plots showing results from simulation give emittance as a function of beam current at the location of the emittance meter, such as in Figure 17. These contain data from simulations which were launched with the input beam current chosen in regular steps for any given curve. These were either 2.5 mA, 5 mA or 10 mA. If no losses occur in the system, the regular steps in input current will correspond to equal steps in the final current, which is the case in Figure 17 between 22.5 mA and 60 mA. In case of losses, points will be displaced horizontally to lower currents relative to where they would be if no losses had occurred. This leads to an increase of the density of points on the graphs. When curves change their direction at high input currents, any further increase in current at the bore leads to a decrease in current measured after the solenoid.

7.1 Shift of the puller electrode

The first option to achieve this goal investigated was shifting the puller electrode towards the plasma electrode, i.e. to decrease $d_{\text{bore,puller}}$. Theoretically, the larger extraction field penetrates further into the plasma region causing the meniscus to become more concave.

In Figure 22a, emittances from simulation are given for distances of 4.5 mm (original value) to 3 mm between the puller electrode tip and the plasma bore. The shorter extraction gap trades beam focusing for initial emittance: the minimal emittance after the gap was

21
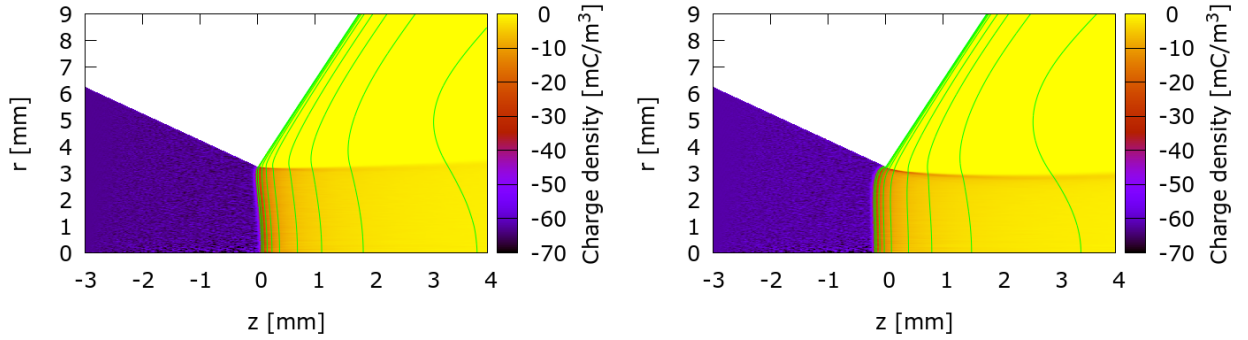
(a) Original configuration: 6.5 cm bore diameter, 4.5 mm puller-bore distance.

(b) Reduced extraction gap: 6.5 cm bore diameter, 3.5 mm puller-bore distance.
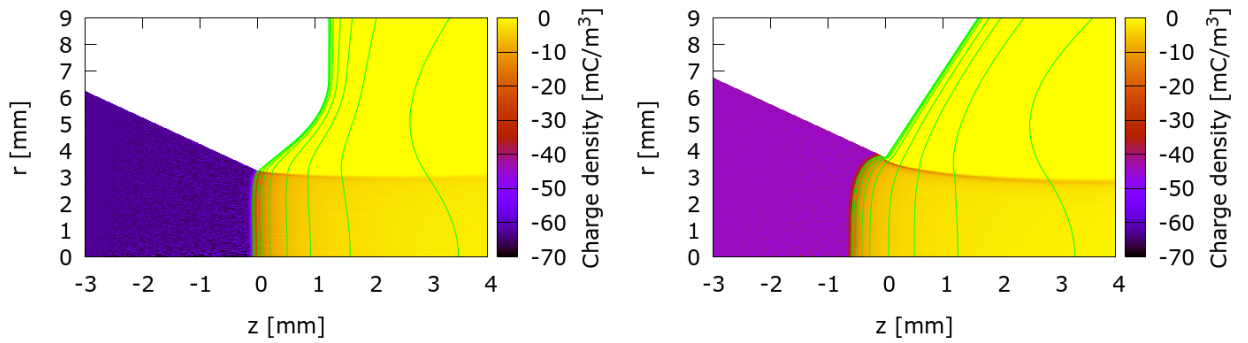
(c) Lower angle electrode: 6.5 cm bore diameter, 3.5 mm puller-bore distance, $\varphi_{\mathrm{plasma}} = 60°$.

(d) Larger bore diameter electrode: 7.5 cm bore diameter, 3.5 mm puller-bore distance.

Figure 21: Plasma meniscus for the original IS03 configuration and for the three different electrode options investigated below. Beam current was 50 mA with no electrons extracted. All three options shift the meniscus into a more concave position compared to the original situation.
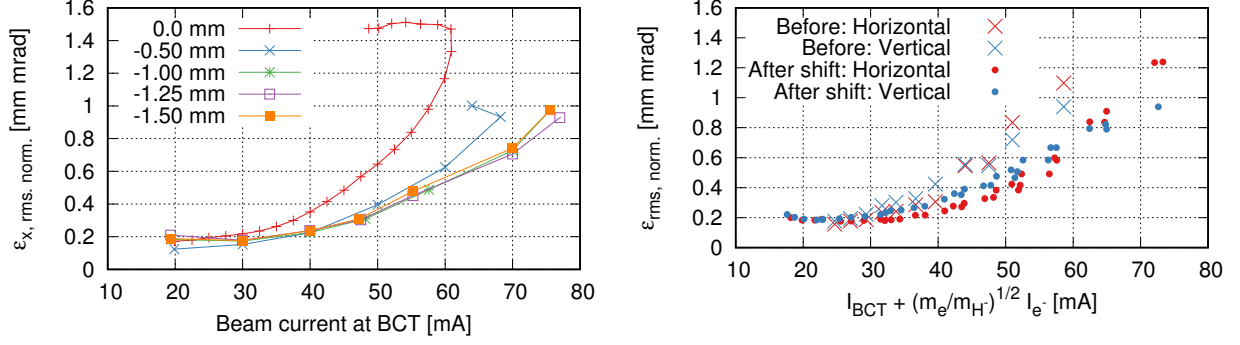
(a) Simulation of the emittance as a function of current at the emittance meter, for e/H=4.

(b) Emittance measurement on an uncesiated source.

Figure 22: Shifting the puller electrode towards the plasma electrode causes the meniscus to become more concave. The additional focusing helps to avoid aberration later on in the extraction system.

always found for the case of a flat meniscus. However, since the measured values for this system are completely dominated by emittance growth after the gap, there is a clear improvement of the emittance at higher currents for shifts up to -1 mm. Larger shifts do not result in further improvements. As a downside, between 40 mA and 70 mA, the modification causes a lower transmission through the solenoid. Putting the puller electrode even closer than 3 mm, results in an increase of the emittance at the location of the emittance meter.

Figure 22b contains results from measurements done on an uncesiated source that was measured twice, once with a puller-plasma bore distance of 4.5 mm and once with 3.5 mm. Since the electron-to-ion ratio was not reproducible between these two configurations, the plot gives the data as a function of space-charge density in the extraction. The behaviour of the simulated and measured curves are remarkably similar. The rms emittances are identical at around 25 mA. As the current is increased, the emittance in the configuration with displaced electrode increases more slowly than in the original system. At 50 mA, both simulation and measurement show an improvement of about 0.2 mm mrad.

The smaller distance of 3.5 mm was kept for the following measurements.

7.2 Plasma electrode angle

Around the bore, the plasma electrode is not flat but is cut at an angle of $\varphi_{\mathrm{plasma}} = 73°$ towards the beam axis. This angle leads to a transverse electric field that provides additional focusing of the extracted beam. According to the simulation, a decrease of the angle, i.e. a stronger transverse field, should improve the emittance since the beam remains smaller in the critical sections downstream.

Figure 23a gives the emittances for an electrode with a decreased angle of 60 deg, with the puller electrode at its original distance and with the puller shifted forward. At the original puller position, the decrease in angle leads to a significant improvement of the beam's emittance. If the puller is positioned 1 mm closer to the plasma electrode, the beneficial effects disappear except for small effects at low beam currents.

23
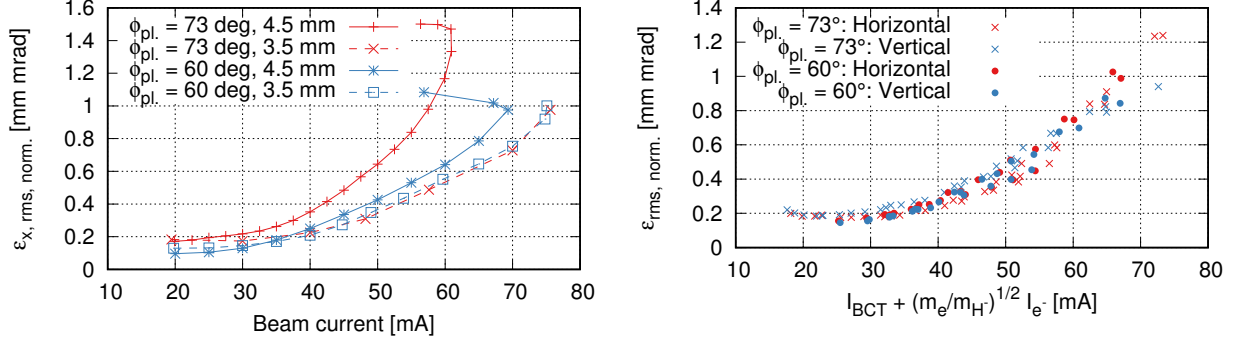
(a) Simulation of the emittance as a function of current at the emittance meter, e/H=2.

(b) Measurement on an uncesiated source.

Figure 23: Decreasing the angle of the plasma electrode towards the beam axis increases transverse beam focusing. There is only a clear improvement in simulation with the original puller-plasma electrode distance which could not be confirmed since both measurements used the new puller-bore distance previously discussed.

The plasma electrode simulated and tested was not identical in design to the standard electrode. The electrode thickness was reduced from $3.2\,\mathrm{mm}$ to $1.2\,\mathrm{mm}$ around the bore to increase the distance to the outside of the puller tip. Additionally, the transition was rounded to decrease the risk of sparking.

The experiment was improperly set up to show the improvements due to the angle since the puller electrode tip was positioned $3.5\,\mathrm{mm}$ behind the plasma bore. Nevertheless, the measured data shown in Figure 23b is consistent with the prediction by the simulation: the emittances compared to a source with the 73° electrode are largely identical.

7.3 Bore diameter

Another possibility is to increase the diameter of the plasma bore. This causes the electric field to extend farther into the plasma region, causing a shift in meniscus. Figure 24 shows the prediction of the rms emittances for different diameters.

In the case of low beam currents, the non-linear focusing effects from the meniscus described in the previous section, cause an increase in the emittance at 20 to $30\,\mathrm{mA}$. This effect gets increasingly stronger with larger diameters and can be mitigated in operation by a decrease in puller voltage. In the intermediate current range between 30 and $50\,\mathrm{mA}$, the simulation predicts that increasing the bore diameter delays the onset of aberration to higher current up to a diameter of $7.5\,\mathrm{mm}$. Increasing the diameter further, the larger emittance predicted by the simulation is due to the increasing importance of aberration at the bore, i.e. can also be avoided by using lower extraction voltages. Above $50\,\mathrm{mA}$, the beam emittance still benefits from a bigger extraction bore. However, the transmission falls below $100\,\%$ due to losses in the solenoid. Nevertheless, the total current output of the source increases.

Figure 25 shows a comparison of emittance measurements from sources with bore diameters of $6.5\,\mathrm{mm}$ and $7.5\,\mathrm{mm}$ (Configuration #2 and #5). (a) contains results from measurements without cesium. Since, in this situation, the electron to ion ratio can not be directly
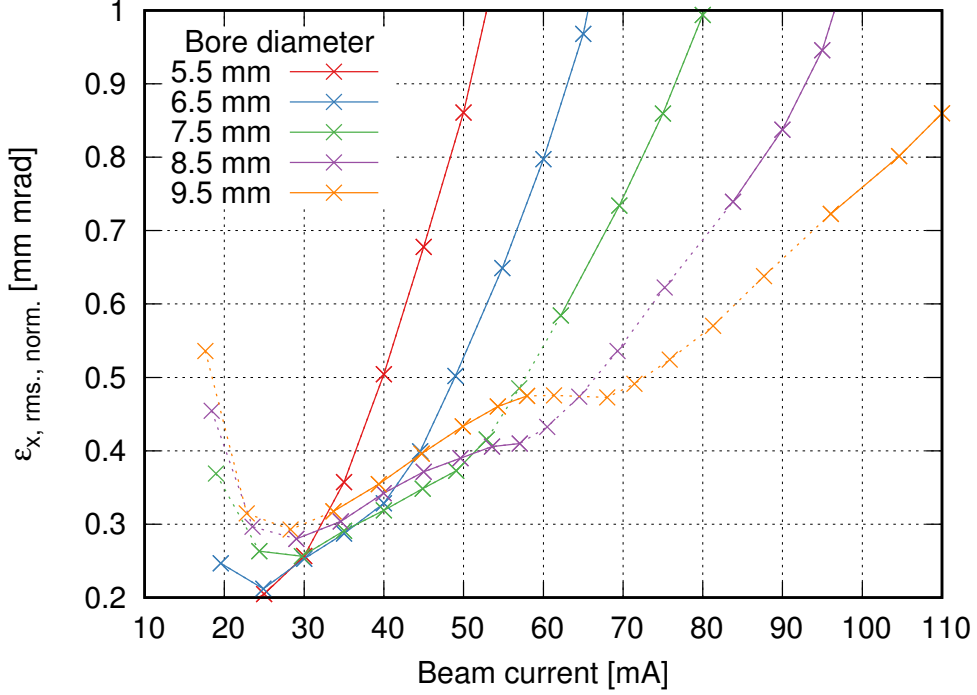
24

Figure 24: Predicted rms emittances at the emittance meter for various plasma bore diameters and beam currents at 10 kV puller voltage. The electron to ion ratio was fixed to be 2. Due to the collimation at the end of the puller-dump electrode, the maximum beam current that can be transported through the extraction also increases.

(a) Uncesiated sources.
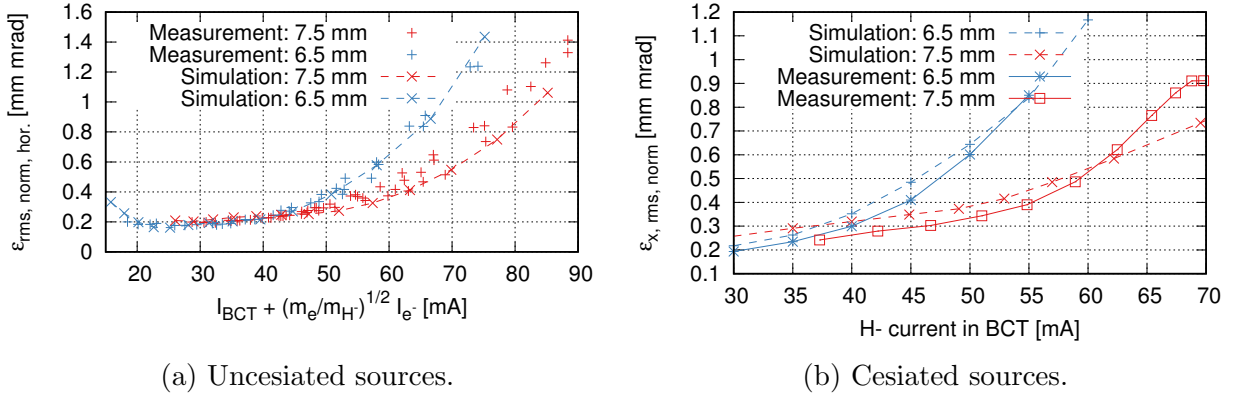

(b) Cesiated sources.

Figure 25: Comparison of measured emittances on uncesiated and cesiated sources as function of beam current. The puller-bore distance was 3.5 mm, except for the measurement of the 6.5 mm bore diameter on the cesiated source (configuration #1). Dashed lines show the prediction by the simulation. Note that the emittance values in (b) are very likely to be at least 10 % too low—and much lower at higher currents—, since the emittance meter bias voltage was not connected at the time of the measurement.

controlled and varied between the two sources, the results are given as a function of the effective extracted current. While the absolute values are different, the relative between the two diameters shows the same qualitative behaviour as predicted by the simulation. Up to 40 mA effective beam current, the emittances for both configurations are identical and then start to diverge. Just as in the simulation, there is then a difference of approximately 0.3 mm mrad between the curves.

Figure 25b contains the same comparison for two cesiated sources: the initial configuration and a source with 7.5 mm and the puller electrode one millimeter closer to the plasma electrode. For the source with 6.5 mm bore diameter, the electron to ion ratio was between 2 and 3, for the source with 7.5 mm between 1 and 2. Since the additional charge density added is small in both cases, the differences should be negligible. For the latter source, additionally, the puller was shifted by 1 mm closer towards the plasma electrode.

There is doubt on the validity of the data—especially those with higher currents—since the emittance meter bias voltage was not connected at the time of the measurement. Values below 55 mA can be expected to be at least 10 % too low, the higher beam currents even farther off.

The simulation predicts a lower transmission due to losses in the first solenoid at higher currents, for example between 50 to 70 mA for a diameter of 7.5 mm. This issue can be observed in scans of the puller voltage. Instead of showing a constant or slightly increasing current after reaching a certain voltage, there is a short plateau and a subsequent drop in the current towards higher voltage, where beam is lost in the solenoid.

While the simulated current limitation at approximately 65 mA for a bore of 6.5 mm was observed in measurements, the source at 7.5 mm was not able to reach the predicted 80 mA. This suggests that the adjustment factor that was previously introduced needs to be adjusted as the diameter is increased. Another possibility is the presence of other effects that were not modeled.

Sources with larger bore diameters will be measured at the test stand in the near future. While these do not offer the same improvements over the whole current range as the upgrade from 6.5 mm to 7.5 mm, i.e. due to the transmission problems and potentially larger emittances at low current, the measurements will be essential as a starting point for a future redesign of the extraction system.

8 Summary and outlook

Linac4's ion source consists of an 2 MHz RF-driven plasma generator, operated with or without the injection of cesium, and a five electrode extraction system. Measurements as a function of various parameters, showed an unexpected strong increase of the emittance towards higher currents and low puller voltage.

We found that the measurement results—extracted currents and emittance—can be well reproduced by simulations using IBsimu. This required solving resolution issues in the area around the meniscus as well as the introduction of a factor increasing the plasma density in the extraction model. Both changes to the simulation cause the plasma meniscus to be more convex and thus, the extracted beam to be more divergent. Downstream, the larger-than-expected beam size results in emittance growth both at the end-plate of the puller-dump

electrode and in the einzel lens due to aberration.

Three modifications to the extraction system were proposed and tested: moving the puller electrode towards the plasma electrode, increasing the diameter of the bore and a smaller angle of the plasma electrode towards the beam axis. The first two options cause the meniscus to become more concave while the third option increases transverse focusing in the extraction gap. Emittance measurements showed the expected effects, both in direction as well as often in magnitude of the change predicted by simulation.

Larger bore diameters will be measured on the Linac4 test stand in the near future. These will provide the basis for further adjustments of the extraction system, and, if not sufficient, for a future redesign of the system.

9 References

[1] J. Lettry et al. "CERN's Linac4 cesiated surface H⁻ source". In: *AIP Conf. Proc.* 1869 (2017), p. 030002. URL: http://cds.cern.ch/record/2286466.

[2] A.M. Lombardi. "Linac4: From Initial Design to Final Commissioning". In: *Proc. of International Particle Accelerator Conference (IPAC'17), Copenhagen, Denmark, 14-19 May, 2017*, pp. 1217–1222. DOI: 10.18429/JACoW-IPAC2017-TUYA1.

[3] G. Bellodi. "Linac4 Commissioning Status and Challenges to Nominal Operation". In: *Proc. 61st ICFA Advanced Beam Dynamics Workshop (HB'18), Daejeon, Korea, 17-22 June 2018*. ICFA Advanced Beam Dynamics Workshop 61, pp. 14–19. DOI: doi:10.18429/JACoW-HB2018-MOA1PL03.

[4] V. Forte et al. "Multi-Particle Simulations of the Future CERN PSB Injection Process with Updated Linac4 Beam Performance". In: *Proc. 61st ICFA Advanced Beam Dynamics Workshop (HB'18), Daejeon, Korea, 17-22 June 2018*. (Daejeon, Korea). ICFA Advanced Beam Dynamics Workshop 61, pp. 278–283. DOI: doi:10.18429/JACoW-HB2018-WEP2PO007.

[5] D. Fink et al. "H⁻ extraction systems for CERN's Linac4 H⁻ ion source". In: *Nuclear Instruments and Methods in Physics Research Section A: Accelerators, Spectrometers, Detectors and Associated Equipment* 904 (2018), pp. 179–187. DOI: 10.1016/j.nima.2018.07.046.

[6] S. Mattei et al. "Numerical simulation of the RF plasma discharge in the Linac4 H⁻ ion source". In: *AIP Conf. Proc.* 1869 (2017), p. 030018. DOI: 10.1063/1.4995738.

[7] A. Ueno et al. "Solving beam intensity bottlenecks and 100 mA operation of J-PARC cesiated RF-driven H⁻ ion source". In: *AIP Conference Proceedings* 2052.1 (2018), p. 050003. DOI: 10.1063/1.5083757.

[8] H. Oguri et al. "Operation status of the J-PARC RF-driven H⁻ ion source". In: *AIP Conference Proceedings* 1869.1 (2017), p. 030053. DOI: 10.1063/1.4995773.

[9] B. X. Han et al. "Emittance characterization of the spallation neutron source H⁻ injector". In: *AIP Conference Proceedings* 1515.1 (2013), pp. 473–480. DOI: 10.1063/1.4792818.

[10] T. Kalvas et al. "IBSIMU: A three-dimensional simulation software for charged particle optics". In: *Review of Scientific Instruments* 81.2 (2010), 02B703. DOI: 10.1063/1.3258608.

[11] Ø. Midttun, S. Stapnes and R. Scrivens. "Improved beam extraction for a negative hydrogen ion source for the LHC injector chain upgrade, Linac4". Nov. 2014. URL: https://cds.cern.ch/record/2233705.

[12] J. B. Lallement et al. "First commissioning experience with the LINAC4 3 MeV front-end at CERN". In: *Proc. of the North American Particle Accelerator NAPAC13*. 2013, pp. 1217–1222. URL: http://cds.cern.ch/record/1699830.

[13] J.B. Lallement. Private Communication. "Compensation degree above 90 % in Figure 8". CERN, Geneva, Switzerland, 2019.

[14] T. Kalvas. "Development and Use of Computational Tools for Modelling Negative Hydrogen Ion Source Extraction Systems". Dec. 2013. ISBN: 978-951-39-5421-5. URL: http://urn.fi/URN:ISBN:978-951-39-5421-5.

[15] J.-B. Lallement et al. "Activities at the Linac4 Test Stand". In: *Proc. 29th Linear Accelerator Conference (LINAC'18), Beijing, China, 16-21 September 2018*. (Beijing, China). Linear Accelerator Conference 29. Aug. 2018, pp. 587–590. DOI: doi:10.18429/JACoW-LINAC2018-TUPO127.

[16] T. Kalvas and J. Lettry. "Deviation of H$^-$ beam extraction simulation model". In: *AIP Conference Proceedings* 2052.1 (2018), p. 050007. DOI: 10.1063/1.5083761.